

Energy shift of Fe-K fluorescence lines due to low ionization demonstrated with XRISM in Centaurus X-3

Yutaro NAGAI ^{1,*}, Teruaki ENOTO ^{1,2,*}, Masahiro TSUJIMOTO ^{3,4}, Hiroya YAMAGUCHI ^{3,4}, Yuto MOCHIZUKI ^{3,4}, Ehud BEHAR ⁵, Lia CORRALES ⁶, Paul A. DRAGHIS ⁷, Ken EBISAWA ³, Natalie HELL ⁸, Timothy R. KALLMAN ⁹, Richard L. KELLEY ⁹, Pragati PRADHAN ¹⁰, Shinya YAMADA ¹¹, Toshiyuki AZUMA ¹² and Xiao-Min TONG ¹³

¹Department of Physics, Graduate School of Science, Kyoto University, Sakyo-ku, Kyoto, Kyoto 606-8502, Japan

²Center for Advanced Photonics, RIKEN, Wako, Saitama 351-0198, Japan

³Institute of Space and Astronautical Science, Japan Aerospace Exploration Agency, Chuo-ku, Sagamihara, Kanagawa 252-5210, Japan

⁴Department of Astronomy, Graduate School of Science, The University of Tokyo, Bunkyo-ku, Tokyo 113-0033, Japan

⁵Physics Department, Technion, Haifa 32000, Israel

⁶Department of Astronomy, University of Michigan, Ann Arbor, MI 48109, USA

⁷MIT Kavli Institute for Astrophysics and Space Research, Massachusetts Institute of Technology, 70 Vassar St, Cambridge, MA 02139, USA

⁸Lawrence Livermore National Laboratory, Livermore, CA 94550, USA

⁹NASA's Goddard Space Flight Center, Greenbelt, MD 20771, USA

¹⁰Department of Physics, Embry-Riddle Aeronautical University, Prescott, AZ 86301, USA

¹¹Department of Physics, Rikkyo University, Toshima-ku, Tokyo 171-8501, Japan

¹²Atomic, Molecular and Optical Physics Laboratory, RIKEN, Wako, Saitama 351-0198, Japan

¹³Center for Computational Sciences, University of Tsukuba, Tsukuba, Ibaraki 305-8573, Japan

*E-mail: nagai.yutaro.25r@st.kyoto-u.ac.jp, enoto.teruaki.2w@kyoto-u.ac.jp

ORCID: 0009-0003-9261-2740, 0000-0003-1244-3100, 0000-0002-9184-5556, 0000-0002-5092-6085, 0000-0003-3224-1821, 0000-0001-9735-4873, 0000-0002-5466-3817, 0000-0002-2218-2306, 0000-0002-5352-7178, 0000-0003-3057-1536, 0000-0002-5779-6906, 0009-0007-2283-3336, 0000-0002-1131-3059, 0000-0003-4808-893X, 0000-0002-6416-1212, 0000-0003-4898-3491

Abstract

The Fe $K\alpha$ fluorescence line at 6.4 keV is a powerful probe of cold matter surrounding X-ray sources and has been widely used in various astrophysical contexts. The X-ray microcalorimeter spectrometer onboard XRISM can measure line shifts with unprecedented precision of ~ 0.2 eV, equivalent to a line-of-sight velocity of ~ 10 km s $^{-1}$. At this level of accuracy, however, several factors that influence the line energy must be carefully considered prior to astrophysical interpretation. One such important factor is the ionization degree, Fe^{q+} . The $K\alpha$ line shifts redward by ~ 4 eV as q increases from 0 (neutral) to 8 (Ar-like). Additionally, the accompanying Fe $K\beta$ line at 7.06 keV shifts blueward by ~ 30 eV from $q = 0$ to 8. We demonstrate that this effect is actually observable in the XRISM data of the high-mass X-ray binary Centaurus X-3 (Cen X-3). We advocate that the differential energy shift between the $K\alpha$ and $K\beta$ line provides a robust estimate of q by decoupling from other effects that shift the two lines in the same direction. We derived $q \sim 5$ (Sc-like) for the fluorescing matter by comparing the observation with atomic structure calculations of our own and in the literature. By accounting for the derived charge state and the corresponding shift in the rest-frame line energy, we made corrections for this effect and reached a consistent residual shift among the $K\alpha$, $K\beta$, and the optical measurement attributable to the systemic velocity of the system. Consequently, we obtained a new constraint on the location of the cold matter. This ionization effect needs to be assessed in all use cases of the Fe $K\alpha$ line shift beyond Cen X-3, and the proposed metric is generally applicable to all of them.

Keywords: atomic processes — X-rays: binaries — stars: neutron — X-rays: individual (Cen X-3)

1 Introduction

The Fe $K\alpha$ fluorescent emission line at 6.4 keV is one of the most widely used diagnostics in X-ray spectroscopy. The emission is produced by radiative decay following the inner-shell ionization of neutral to low-ionized Fe^{q+} (typically below Ar-like with an ionization degree $q \leq 8$, where $q = 0$ is for neutral) in cold matter. The ionization source can be photons or charged particles above the threshold energy of 7.11 keV. The line carries information about the ionizing source, the cold matter, and the relation between them through its observed properties: i.e., the intensity or the equivalent

width (EW), the energy shift, and the line profile. Due to the rich cosmic abundance of Fe, the large fluorescence yield (0.355; Firestone & Shirley 1996), and the sufficiently high energy to penetrate through the interstellar extinction of $N_H \sim 10^{22}$ cm $^{-2}$, the line has profound utility in almost all fields of X-ray astronomy (Kaastra 1999).

The utility is further enhanced by the advent of the X-ray microcalorimeter spectrometer onboard the X-Ray Imaging and Spectroscopy Mission (XRISM; Tashiro et al. 2025). With the superb spectroscopic performance of the *Resolve* instrument (Kelley et al. 2025; Ishisaki et al. 2025), the Fe $K\alpha$ line is used in ways that

were never possible with previous CCD and grating spectrometers. The two intense lines of the complex ($K\alpha_1$ and $K\alpha_2$ respectively at 6.404 and 6.391 keV for $q = 0$) were resolved (Miller et al. 2025; Bogensberger et al. 2025); the weak satellite lines ($K\alpha_{3,4}$ at 6.435 keV) were detected (Vander Meulen et al. in preparation); the bulk velocity of <100 km s $^{-1}$ was derived (Chakraborty et al. 2025); the radial velocity (RV) curve of a wide binary was obtained (Nazé et al. submitted); Doppler tomography was applied (Sameshima et al. submitted); the multiple components of different broadening were separated (Kammoun et al. 2025; XRISM Collaboration et al. 2024); and the timing of the line photons relative to the continuum photons was constrained (Mochizuki et al. 2024).

These novel applications remind us that we need to know the intrinsic properties of the line to the accuracy that the microcalorimeter spectra can achieve. Such caution is most evident in the result of the *Resolve* observation of the X-ray binary Centaurus X-3 (Cen X-3). Mochizuki et al. (2024) revealed that the line energy is modulated by the binary orbital motion. The RV curve of the line is consistent with the NS motion in phase but with a slightly smaller amplitude than expected. However, the most striking result is the measured RV offset of -140 ± 4 km s $^{-1}$, which was very tightly constrained by observing the RV curve over the entire phase. The magnitude of the shift (equivalent to 470 ppm at 6.4 keV) is significantly larger than all conceivable sources of systematics, including the systemic velocity of the system derived from optical spectra of the O star (130 ppm; Hutchings et al. 1979), the energy determination accuracy of *Resolve* (30 ppm; Porter et al. 2025; Eckart et al. 2025), the Earth's orbital motion around the Sun (51 ppm), and the Sun's motion with respect to the local standard of rest (17 ppm) at the time of the observation.

It is obvious that we need to revisit the assumptions regarding the intrinsic properties of the line based on atomic physics. In particular, the assumption that the line is from neutral ($q = 0$) Fe can lead to incorrect conclusions, as the line energy can shift by ~ 4 eV (625 ppm) when Fe is ionized to $q = 8$ (Palmeri et al. 2003). The purpose of this paper is to demonstrate, for the first time, that this effect actually occurs using the same Cen X-3 data with *Resolve*. A robust assessment is achieved by combining it with the accompanying $K\beta$ fluorescence line at 7.06 keV, which became accessible with *Resolve* without contamination from the K edge feature at 7.11 keV. As we will show in this paper, the differential energy shift between the $K\alpha$ and $K\beta$ lines behaves distinctly differently from other sources of systematics. By taking this effect into account properly, we further show that the systemic velocity of the system can be better reconciled among different results, and the average q value can be derived, which provides new constraints on the fluorescing matter and its ionizing source.

The outline of this paper is as follows. We start with a brief description of the target, the instrument, the observation, and the data reduction in section 2. A more detailed description can be found in the preceding paper (Mochizuki et al. 2024). We present the results of the data analysis in section 3, in which we characterize the observed $K\alpha$ and $K\beta$ lines. In section 4, we evaluate the atomic effects for the line energy shifts (subsection 4.1). We further discuss new constraints on fluorescing matter in the Cen X-3 system (subsection 4.2). We summarize our findings and conclude with their astrophysical implications in section 5.

All errors throughout the paper are given for the 1σ statistical uncertainty. We take RV redshifts (lower shift in energy) as negative values to align with the preceding work (Mochizuki et al. 2024), although this is contrary to astronomical conventions.

2 Data

Cen X-3 is an eclipsing high-mass X-ray binary with an orbital period of 2.09 days. It is composed of a neutron star (NS) and an O6–8 III giant V779 Cen (Krzeminski 1974; Hutchings et al. 1979). The XRISM observation was performed to cover an entire orbital phase from February 13 to 16, 2024. The dates were chosen so that the target could be observed with minimum interruption, with no Earth occultation seen from XRISM orbiting the Earth in a precessing plane. As a consequence, the line-of-sight velocity of XRISM around the Earth was very small at 0.5 km s $^{-1}$ (1.7 ppm) in peak-to-peak. The basic properties of the system and the observation are tabulated in table 1. Compared to other X-ray observations in the past (Naik, Paul, & Ali 2011; Sanjurjo-Ferrín et al. 2021; Tamba et al. 2025), the X-ray flux remained relatively stable over an entire orbit outside of eclipses, making it easy to interpret the observed RV curve.

We use the *Resolve* instrument aboard XRISM (Kelley et al. 2025; Ishisaki et al. 2025). It hosts an array of 6×6 X-ray microcalorimeter pixels (pixels 0–35) placed at the focal plane of the X-ray mirror assembly. One of the pixels (pixel 12) is displaced from the array for calibration purposes. When all the array pixels are combined, it has a spectral resolution of $R \equiv E/\Delta E = 1300$ (Porter et al. 2025) and an effective area of 180 cm 2 (Hayashi et al. 2024) at 5.9 keV, a band-pass coverage of 1.7–12 keV, a very low background equivalent to $\lesssim 0.5$ events per 5 eV for a 100 ks exposure (Mochizuki et al. 2025a), and a $3' \times 3'$ field of view with a point spread function of 1.3'. The spectroscopic performance surpasses those of any previous spectrometers at the Fe K band, but the true uniqueness of *Resolve* is its energy determination accuracy of $\lesssim 0.2$ eV at 5.9 keV (Porter et al. 2025). It is achieved by careful design of the instrument and the operation unseen in other high-resolution X-ray spectrometers; i.e., the ^{55}Fe calibration sources are illuminated intermittently during observations, and every individual event is assigned energy based on the energy gain variation model derived for each pixel for each observation^a.

We started with the pipeline products using processing version 03.00.011.008. For data editing and calibration, we used HEASoft software build 7 and the calibration database (CALDB) version 20230815. We restricted ourselves to using events of the Hp grade, which are isolated in time from other events in the same pixel and thus are best calibrated for spectroscopic purposes (Porter et al. 2025; Eckart et al. 2025). We also applied additional screening based on the pulse height and rise time of X-ray events (Mochizuki et al. 2025a) and removed events from pixel 27, which is known to sometimes behave anomalously in the energy gain variation. Outside the eclipse ($\phi_{\text{orb}} = 0.16\text{--}0.87$), the count rate in the 1.7–12 keV band is ~ 30 s $^{-1}$ and the Hp branching ratio is $\sim 40\%$. The contributions from any contaminating source and background events are negligible.

3 Analysis

3.1 Light curve and broadband spectra

Figure 1 (a) shows the *Resolve* light curves covering the 2.09-day entire orbit of Cen X-3. Here, the phase origin is defined at the middle of the eclipse based on the ephemeris by Falanga et al. (2015). We defined three phases: $\phi_{\text{orb}} = 0.16\text{--}0.5$ (ϕ_1 ; 51.5 ks) when the NS is approaching us, $\phi_{\text{orb}} = 0.5\text{--}0.87$ (ϕ_{II} ; 48.7 ks)

^a A report for the present observation can be found in https://heasarc.gsfc.nasa.gov/FTP/xrism/postlaunch/gainreports/3/300003010_resolve_energy_scale_report.pdf.

when the NS is retreating from us, both outside of the eclipse, and $\phi_{\text{orb}} = -0.08\text{--}0.09$ and $0.89\text{--}0.97$ (ϕ_{III} ; 43.0 ks) in the eclipses. Some dipping behavior was observed at $\phi_{\text{orb}} = 0.14$ and 0.61 for ~ 5 ks and ~ 9 ks, respectively. These events will be described in a separate paper (Loberger et al. in preparation), but are excluded from the present analysis.

The broadband spectra in each phase are shown in figure 2 (a). The spectra in (ϕ_{III}) and out (ϕ_1 and ϕ_{II}) of the eclipse are drastically different, while the two spectra in the former (ϕ_1) and the latter (ϕ_{II}) half out of the eclipse are similar except for a minor difference in the flux. We generated the detector and mirror responses using the `rslmkrmf` and `xaarfgen` tools. In the line spread function, the Gaussian core, its exponential tail, the Si $\text{K}\alpha$ instrumental line, and the escape peaks were included (Leutenegger et al. 2025).

Using these responses, we fitted the out-of-eclipse spectra ($\phi_{\text{orb}} = 0.16\text{--}0.87$ except for $0.59\text{--}0.63$) in the $2.0\text{--}12$ keV energy range. A phenomenological model consisting of a power-law continuum attenuated by an interstellar extinction described the continuum spectra reasonably well. The best-fit parameters are the power-law photon index 1.37 ± 0.03 , the absorption column $(3.22 \pm 0.03) \times 10^{22} \text{ cm}^{-2}$, and the $2.0\text{--}12$ keV band luminosity $(2.82 \pm 0.01) \times 10^{37} \text{ erg s}^{-1}$.

3.2 Fe $\text{K}\alpha$ and $\text{K}\beta$ lines

Figure 2 (b) shows an enlarged view of the spectra around the Fe K band. In all three phases, the Fe $\text{K}\alpha$ and $\text{K}\beta$ fluorescence lines as well as the Fe XXV $\text{He}\alpha$ and Fe XXVI $\text{Ly}\alpha$ line complexes were detected. The $\text{He}\alpha$ complex is resolved into four principal lines of w , x , y , and z , while the $\text{Ly}\alpha$ complex is into the spin-orbit doublet of $\text{Ly}\alpha_1$ and $\text{Ly}\alpha_2$. Diagnostics using these lines from highly-ionized Fe are presented in Gunasekera et al. (2025); Mochizuki et al. (2025b). We focus on the fluorescence lines in this paper.

We characterized the near-neutral Fe $\text{K}\alpha$ and $\text{K}\beta$ lines of the three phases (figure 3), by applying the phenomenological model (Hölzer et al. 1997) that is most widely used for the fluorescence line of neutral Fe. The model consists of seven Voigt components for $\text{K}\alpha$ ($\alpha_{11}\text{--}\alpha_{14}$ and $\alpha_{21}\text{--}\alpha_{23}$) and four for $\text{K}\beta$ ($\beta_a\text{--}\beta_d$). Among them, we hereafter use the component corresponding to $\text{K}\alpha_1$ ($2p_{3/2} \rightarrow 1s$) or $\text{K}\beta_1$ ($3p_{3/2} \rightarrow 1s$)^b to represent the energy of each line.

We fitted the narrow-band spectra: 6.3–6.5 and 7.0–7.1 keV for the $\text{K}\alpha$ and $\text{K}\beta$ line, respectively. For each line, we fixed the relative energy and intensity of all components and fitted their energy shift and normalization collectively. For the width of the Voigt profile, we fixed the Lorentz width of each component and fitted the Gaussian width collectively for all components. To account for the underlying continuum, we added a constant offset. This approach was successful, yielding a statistically-acceptable fit for all three phases. There are some residuals in the line profile, but the line centroid is tracked well enough. The best-fit parameters are summarized in table 2.

When the energy shifts are interpreted solely due to the Doppler effect, we derived their RV as a function of the orbital phase (figure 1b). The richer statistics of the $\text{K}\alpha$ line allowed us to conduct the spectral fitting in a finer phase binning than in three. We obtained a sinusoidal curve for $\text{K}\alpha$ consistent with the previous work (Mochizuki et al. 2024), including the RV offset of $-139 \pm 15 \text{ km s}^{-1}$. The RV curve of $\text{K}\beta$ was presented here

for the first time. The data points are too sparse to obtain the amplitude and phase shift, but its RV offset was constrained to $345 \pm 60 \text{ km s}^{-1}$, which is vastly different from that of $\text{K}\alpha$.

4 Discussion

4.1 Ionization effect of the line energy

The fact that the $\text{K}\alpha$ and $\text{K}\beta$ lines exhibit different RV offsets is very peculiar. This makes it unlikely that the shifts are dominated by any common-mode shifts acting on both lines in the same direction, such as residual Doppler shifts. Rather, it points toward the origins in atomic physics. In fact, such a differential-mode shift is expected for low-ionized Fe (figure 4). From $q = 0$ to 2, the energies of the $\text{K}\alpha$ and $\text{K}\beta$ lines are almost constant. From $q = 3$ to 8, the energy of the $\text{K}\alpha$ line shifts monotonically redward by $\sim 4 \text{ eV}$ (equivalent to -200 km s^{-1}), while that of the $\text{K}\beta$ line shifts blueward by $\sim 30 \text{ eV}$ ($+1300 \text{ km s}^{-1}$).

A simplified explanation of this effect is as follows (Griffin, Andrew, & Cowan 1969). For $q = 1$ and 2, the electrons in the $4s$ orbital are removed, one by one, which has little impact on the $3p$ and $2p$ orbitals. For $q = 3$ to 8, electrons in the $3d$ orbital are removed. The average radius of the $3d$ orbital is close to that of the $3p$ orbital. As q increases, the energy level of the $3p$ orbital increases due to the decreasing Debye shielding of the nuclear charge. This causes the energy of the $\text{K}\beta$ line (the transition from $3p$ to $1s$) to increase monotonically. In contrast, the average radius of the $3d$ orbital is larger than that of the $2p$ orbital. As q increases, the $3d$ orbital shrinks due to reduced repulsion among electrons in the $3d$ orbital, thus the energy level of the $2p$ orbital decreases due to increased Debye shielding. This makes the energy of the $\text{K}\alpha$ line (the transition from $2p$ to $1s$) decrease monotonically.

Laboratory experiments to determine the line energies of $\text{K}\alpha$ and $\text{K}\beta$ for low-ionized Fe ($q \geq 1$) are not available in the literature. We need to rely on atomic structure calculations, which have their own systematic uncertainties. To assess their magnitude, we used the results of two calculations of different solvers. One is from the literature (Palmeri et al. 2003) based on the Hartree-Fock (HF) approximation with relativistic corrections. The other is our own calculation based on the density functional theory (DFT), or more specifically, the relativistic local-spin density approximation with self-interaction correction (RLSDA/SIC; Perdew & Zunger 1981).

The numerical procedures of the HF and DFT are similar, as both solve the single-electron time-independent Schrödinger equation self-consistently. The difference lies in how to construct the effective potential. The HF potential considers the electron-exchange effect exactly while ignoring the electron-correlation effect completely, whereas the DFT potential accounts for both effects using the local density approximation (Kotochigova et al. 1997). The total energy (the energy of the entire atomic system with a specific electron configuration, including the electron kinetic energy, the electron–nucleus interaction, the electron–electron Coulomb repulsion, and an approximate exchange–correlation contribution in the DFT, and the exchange-only contribution in the HF) is consistently better in the DFT over HF calculations (table I in Tong & Chu 1997). The orbital energy (the energy of an electron occupying a particular orbital within the effective potential) is also improved in the DFT over the HF calculations (Tong & Chu 1998). We present our DFT results in table 3.

Still, the absolute energy of the DFT calculations is not sufficiently accurate for the present application. The calculated values (6395.31 and 7050.87 eV for the neutral Fe $\text{K}\alpha_1$ and $\text{K}\beta_1$,

^b For $\text{K}\alpha_1$, it is $\text{K}\alpha_{11}$ in table II and figure I (c) in Hölzer et al. (1997). For $\text{K}\beta_1$, it is $\text{K}\beta_c$ in their table III or $\text{K}\beta_a$ in figure I (d); a typo was noted in the $\text{K}\beta$ nomenclature.

respectively) are consistently lower than the experimental values (6403.84 and 7057.98 eV; Bearden 1967). The discrepancy amounts to 7–8 eV. Thus, we use the differential energies to be more robust against systematic uncertainty. Assume that $E_{K\alpha_1}(q)$ and $E_{K\beta_1}(q)$ are the calculated energy of the $K\alpha_1$ and $K\beta_1$ lines of Fe^{q+} , respectively. We take the difference in two ways: one is the difference against $q = 0$ as $\Delta E_{K\alpha_1}(q) \equiv E_{K\alpha_1}(q) - E_{K\alpha_1}(0)$ and $\Delta E_{K\beta_1}(q) \equiv E_{K\beta_1}(q) - E_{K\beta_1}(0)$ and the other is the difference between the two lines of the same q as $\Delta E_{K\alpha_1\beta_1}(q) \equiv E_{K\alpha_1}(q) - E_{K\beta_1}(q)$. For $q = 0$, $\Delta E_{K\alpha_1\beta_1}(0)$ is much more consistent between the calculation (655.56 eV) and the experiment (654.14 eV) within 1.42 eV. For $q > 1$, we have no experimental values to compare, but the difference between the two calculations is small enough for the present application to distinguish $q \sim 0$ from $q > 3$, justifying its use. This is reasonable considering the decreased impact of the exchange and correlation effects among electrons as q increases.

Figure 4 shows (a) $\Delta E_{K\alpha_1}(q)$, (b) $\Delta E_{K\beta_1}(q)$, and (c) $\Delta E_{K\alpha_1\beta_1}(q)$ as functions of q from the two calculations. We compared them with the RV offset measured for the two lines and their differences. In panel (c), the measured energy shift is most consistent with $q = 5$ (Sc-like) for all three metrics, two of which are independent from each other. The value of $\Delta E_{K\alpha_1\beta_1}$ is also consistent among the three different phases of 664.9 ± 1.4 eV (ϕ_I), 668.9 ± 1.1 eV (ϕ_{II}) and 666.6 ± 1.9 eV (ϕ_{III}), demonstrating that the metric is robust against varying RV shifts due to orbital motion and can be applied even if the complete RV curve is unavailable.

In reality, we would expect some distribution in the charge state, and we consider that $q = 5$ represents the average. We use the single value for the assessments below. Taking into account the energy shift due to the ionization effect, we revised the RV curve modeling in figure 1 (c) assuming $q = 5$. The revised RV offset is -50 ± 15 km s $^{-1}$ for $K\alpha$ and -66 ± 61 km s $^{-1}$ for $K\beta$, which are now consistent with each other and also with the optical measurement of -39 km s $^{-1}$ (Hutchings et al. 1979). This further reinforces our claim that the measured line energies of $K\alpha$ and $K\beta$ are affected by the ionization effect of $q \sim 5$.

To be self-consistent, we performed the spectral fitting in subsection 3.2 by assuming that the lines are from Fe VI, instead of Fe I, by referring to their line properties in table 3. We confirmed that, after applying this ionization correction, the inferred average q and RV offset remain the same within the statistical uncertainty.

4.2 New constraint on the fluorescing material

We obtained the average q in the course of explaining the observed discrepancy in the RV offset. As a byproduct, we can obtain a new constraint on the fluorescing material in the Cen X-3 system. The inner-shell ionization source should be the NS for having sufficient high-energy photons above the K edge energy, but the ionization source for the fluorescent material up to $q = 5$ can be different. One is the O star itself and the other is the NS contributing also for low-ionization. From the amplitude of the RV curve, Mochizuki et al. (2024) argued that the location of the fluorescing material is close to the first Lagrange (L_1) point. They also examined whether their model can reproduce the observed equivalent width and line width of the Fe $K\alpha$ line as a function of the orbital phase. In this work, we examine how the newly constrained ionization degree q can contribute to further constraining such models. To this end, we perform a simple calculation to test whether the two candidate ionization sources are both consistent with the derived value of q , and show that both scenarios remain plausible.

The first is the O star. The effective temperature of 3.5×10^4 K (Hutchings et al. 1979) for a O6–8 giant appears too low (photon spectrum peaking at 5 eV) to cause ionization up to $q = 5$ requiring 99 eV (Kramida et al. 2024), but because of non-local thermodynamic equilibrium (NLTE) effects, this is possible at the surface. Lanz & Hubeny (2003) conducted a radiative transfer calculation using the TLUSTY code for a single O star atmosphere under hydrostatic equilibrium. Figure 5 shows the result of the calculation, in which (a) the Fe charge state distribution, (b) electron density, (c) temperature, and (d) the Fe K optical depth (τ_{FeK}) are shown as a function of the Rosseland optical depth (τ_{Ross}) as a proxy for the geometrical depth (z) from the surface. We added (d) by

$$\tau_{FeK}(z) = A_{Fe} \sigma_{FeK} \int_0^z n_H(z) dz, \quad (1)$$

in which n_H is the H number density, $A_{Fe} = 6.7 \times 10^{-5}$ is the Fe abundance relative to H (Wilms et al. 2000), and $\sigma_{FeK} = 3.8 \times 10^{-20}$ cm $^{-2}$ is the photo-electric absorption cross section at the Fe K edge for the neutral Fe (Berger et al. 2010). The fluorescent lines are expected to be produced most efficiently at $\tau_{FeK} \sim 1$ corresponding to $\tau_{Ross} \sim 1$ (figure 5d). At the depth, the charge state distribution is mostly populated by Fe of $q = 4$ –6 (figure 5a).

The second is the NS. X-ray photons contribute to the photoionization of Fe in materials close to L_1 . This can be assessed using the ionization parameter (Tarter, Tucker, & Salpeter 1969) defined as

$$\xi \equiv \frac{L}{n_e r^2} \text{ erg cm s}^{-1}, \quad (2)$$

where L (erg s $^{-1}$) is the luminosity in 1–1000 Ryd of the ionizing source, n_e (cm $^{-3}$) is the electron density of the ionized matter, and r (cm) is the distance between the ionizing source and the ionized matter. We calculated the radiative transfer using the XSTAR code (Kallman & Bautista 2001) to obtain the charge state distribution of Fe as a function of ξ (figure 6). In the calculation, we assumed that the spectral shape of the NS is represented by a power-law of a photon index of 1.4 (subsection 3.1) and the incident emission went through the stellar wind represented by a slab of a column having 10 22 cm $^{-2}$ before reaching the O star surface. Note that the column is sufficiently thin ($\tau_{FeK} \sim 10^{-2}$) for the inner-shell ionizing photons. The maximum formation of Fe at $q = 5$ is achieved around $\log_{10} \xi = 0$. For $L = 3.2 \times 10^{37}$ erg s $^{-1}$ from the observation (subsection 3.1) and $r = 4.4 R_\odot$ for the distance from the NS to the L_1 point, this converts to $n_e \sim 3 \times 10^{14}$ cm $^{-3}$. This density is achieved again at $\tau_{Ross} \sim 1$ (figure 5b), suggesting that photoionization by NS can also contribute for the ionization to $q \sim 5$.

5 Conclusions and Prospects

The Fe $K\alpha$ fluorescence line at 6.4 keV is widely used in X-ray spectroscopy. The diagnostic is used for the X-ray microcalorimeter data in ways that were never possible before. We need to know the intrinsic properties of the line to the accuracy that the XRISM data can achieve. One caution was found in the RV curve of Cen X-3, in which the RV offset of $K\alpha$ is significantly larger than the optical measurement and is inconsistent with that of $K\beta$. We revisited the assumption that these lines are produced by neutral ($q = 0$) Fe. As the ionization increases, the $K\alpha$ line shifts redward while the $K\beta$ line shifts blueward. This differential shift is distinctive to the ionization effect, and we used the energy difference as a metric to constrain the most likely charge state. By applying the method, we constrained $q \sim 5$. By correcting the line shift of the $K\alpha$ and

$K\beta$ lines, we solved the discrepancy in the RV offset of Cen X-3. This demonstrates that (1) the ionization effect is actually observable in microcalorimeter data and (2) the differential shift between the $K\alpha$ and $K\beta$ lines serves as a robust metric of the effect.

The ionization effect should occur and should be assessed in all use cases of Fe $K\alpha$ diagnostics beyond Cen X-3. An example is the immediate post-shock plasmas in supernova remnants. One can constrain both the bulk motion and the charge state of the shocked plasma, thereby providing valuable insights into the efficiency of collisionless electron heating (e.g., Yamaguchi et al. 2014). Another example is the Fe $K\alpha$ line from the surfaces of compact objects such as white dwarfs. One can constrain the gravitational redshift, which thereby offers a means to constrain the mass of compact objects (e.g., Hayashi et al. 2023). The proposed metric of the differential shift between the $K\alpha$ and $K\beta$ lines will be generically useful in all these cases.

Acknowledgments

We express our gratitude to all scientists and engineers for their persistent efforts to make XRISM possible, following the previous X-ray microcalorimeter missions onboard Astro-E, Suzaku, and Hitomi in international collaborations. Y. N. is supported by the JST SPRING program (grant number JPMJSP2110), T. E. by the JST Sohatsu program (grant number JPMJFR202O), H. Y. by JSPS KAKENHI (grant number 22H00158), Y. M. by the JST SPRING program (grant number JPMJSP2108) and JSPS KAKENHI (grant number JP25KJ0923), E. B. by the Israel Science Foundation (grant number 2617/25), and L. C. by NASA (grant number 80NSSC18K0978, 80NSSC20K0883, and 80NSSC25K7064). N. H.'s work was performed under the auspices of the U.S. Department of Energy by Lawrence Livermore National Laboratory under Contract DE-AC52-07NA27344.

Table 1. Summary of the system parameters of Cen X-3 and the XRISM observation.

Parameter	Symbol	Value	Reference
Binary system parameters			
Mass of the primary star	M_*	$20.5 \pm 0.7 M_{\odot}$	Ash et al. (1999)
Radius of the primary star	R_*	$11.8 R_{\odot} = 8.22 \times 10^{11} \text{ cm}$	Wojdowski, Liedahl, & Sako (2001)
Spectral type of the primary star	—	O6–O8 (f)	Hutchings et al. (1979)
Surface temperature of the primary star	T_*	$35000 \pm 2000 \text{ K}$	Hutchings et al. (1979)
Bolometric luminosity of the primary star	L_*	$\sim 1.9 \times 10^5 L_{\odot} = 7.2 \times 10^{38} \text{ erg s}^{-1}$	derived using the Stefan–Boltzmann law
Mass of the NS	M_x	$1.21 \pm 0.21 M_{\odot}$	Ash et al. (1999)
Spin period of the NS*	P_s	4.791852 s	this work
Orbital period	P_{orb}	$2.08704106 \pm 0.00000003 \text{ days}$	Falanga et al. (2015)
Binary separation	a	$18.14 R_{\odot}$	Bildsten et al. (1997)
Lagrange point L_1 distance from the NS	—	$\sim 4.4 R_{\odot}$	derived using Eggleton (1983)
Inclination angle	i	(70.2 ± 2.7) degree	Ash et al. (1999)
Distance	d	6.4 kpc	Tsygankov et al. (2022)
Systemic velocity**	γ	-39 km s^{-1}	Hutchings et al. (1979)
Position (equinox J2000.0)	(RA, Dec)	(170.3128° , -60.6237°)	
Observation summary of XRISM			
ObsID		300003010	
Start and end of observations		2024-02-12 23:56:04 to 2024-02-15 06:19:04 UT	
Observation duration in orbital phase	ϕ_{orb}	$-0.08 \text{ to } 0.97$	
Total exposure time		196 ks	
2.0–12 keV X-ray flux†	F_x	$(4.858 \pm 0.004) \times 10^{-9} \text{ erg s}^{-1} \text{ cm}^{-2}$	
2.0–12 keV X-ray luminosity†	L_x	$(2.82 \pm 0.01) \times 10^{37} \text{ erg s}^{-1}$	
Radial velocity (RV) curve with $K\alpha$			
RV amplitude		$263 \pm 20 \text{ km s}^{-1}$ (5.60 \pm 0.43 eV in energy)	this work
RV offset ($q = 0$)‡		$-139 \pm 15 \text{ km s}^{-1}$ (-3.0 ± 0.3 eV in energy)	this work
RV offset ($q = 5$)§		$-50 \pm 15 \text{ km s}^{-1}$ (-1.1 ± 0.3 eV in energy)	this work

* The spin period at MJD 60353.

** The binary system is receding from us.

† The absorbed flux and unabsorbed luminosity are the values in the 2–12 keV band during the out-of-eclipse except dip phases.

‡ Assuming that the line is emitted from neutral Fe ($q = 0$).§ Assuming that the line is emitted from Sc-like Fe ($q = 5$).**Table 2.** Best-fit parameters of the Fe $K\alpha_{11}$ and $K\beta_c$ lines using the Hölzer et al. (1997) model.

Line†	Ref. Energy† (eV)	Det. Energy‡ (eV)	Velocity§ (km s^{-1})	Width (eV)	Flux* ($\text{ph s}^{-1} \text{ cm}^{-2}$)	EW* (eV)
$\phi_{\text{I}} = 0.16\text{--}0.5$						
Fe $K\alpha_{11}$	6404.15	$6404.7^{+0.4}_{-0.4}$	$(+2.6^{+1.8}_{-1.8}) \times 10^1$	$8.4^{+0.6}_{-0.6}$	$(2.9^{+0.1}_{-0.1}) \times 10^{-4}$	$4.8^{+0.2}_{-0.1}$
Fe $K\beta_c$	7058.36	$7068.3^{+1.3}_{-1.4}$	$(+4.2^{+0.6}_{-0.6}) \times 10^2$	4^{+2}_{-2}	$(2.8^{+0.6}_{-0.6}) \times 10^{-5}$	$0.5^{+0.1}_{-0.1}$
$\phi_{\text{II}} = 0.5\text{--}0.87$						
Fe $K\alpha_{11}$	6404.15	$6398.1^{+0.4}_{-0.4}$	$(-2.9^{+0.2}_{-0.2}) \times 10^2$	$7.6^{+0.6}_{-0.6}$	$(2.8^{+0.1}_{-0.1}) \times 10^{-4}$	$4.8^{+0.2}_{-0.1}$
Fe $K\beta_c$	7058.36	$7065.5^{+2.5}_{-1.1}$	$(+3.0^{+0.5}_{-1.1}) \times 10^2$	< 5.2	$(2.1^{+0.7}_{-0.5}) \times 10^{-5}$	$0.4^{+0.1}_{-0.1}$
$\phi_{\text{III}} = -0.08\text{--}0.09, 0.89\text{--}0.97$						
Fe $K\alpha_{11}$	6404.15	$6401.0^{+0.5}_{-0.4}$	$(-1.5^{+0.2}_{-0.2}) \times 10^2$	$4.9^{+0.5}_{-0.5}$	$(2.4^{+0.1}_{-0.1}) \times 10^{-5}$	23^{+2}_{-2}
Fe $K\beta_c$	7058.36	$7066.3^{+2.1}_{-1.8}$	$(+3.4^{+0.8}_{-0.9}) \times 10^2$	< 5.3	$(1.6^{+0.6}_{-0.5}) \times 10^{-6}$	$2.4^{+0.8}_{-0.9}$

† Reference energy (Hölzer et al. 1997). In this referenced model, the Fe $K\alpha$ and Fe $K\beta$ lines are approximated by seven and four Voigt functions, respectively. Among these components, the strongest ones are the Fe $K\alpha_{11}$ and Fe $K\beta_c$ lines, respectively.

‡ Observed energy derived by the fitting.

§ The velocity when the energy shift is interpreted solely due to the Doppler shift.

* Values of $K\alpha_{11}$ and $K\beta_c$ only, not the entire complex.

Table 3. Fe K line[†] energies and Einstein A coefficients calculated with the RLSDA/SIC method.

q	$E_{K\alpha_1}$ (eV)	$E_{K\alpha_2}$ (eV)	$E_{K\beta_1}$ (eV)	$E_{K\beta_3}$ (eV)	$A_{K\alpha_1}$ (s^{-1})	$A_{K\alpha_2}$ (s^{-1})	$A_{K\beta_1}$ (s^{-1})	$A_{K\beta_3}$ (s^{-1})
0	6395.31	6382.37	7050.87	7049.27	1.70721×10^{14}	1.74333×10^{14}	2.04859×10^{13}	2.08614×10^{13}
1	6395.51	6382.57	7051.06	7049.47	1.70741×10^{14}	1.74354×10^{14}	2.04545×10^{13}	2.08293×10^{13}
2	6395.77	6382.83	7051.42	7049.82	1.70773×10^{14}	1.74386×10^{14}	2.04297×10^{13}	2.08026×10^{13}
3	6395.28	6382.34	7053.96	7052.31	1.70709×10^{14}	1.74321×10^{14}	2.10084×10^{13}	2.13679×10^{13}
4	6394.76	6381.81	7057.59	7055.87	1.70645×10^{14}	1.74253×10^{14}	2.18021×10^{13}	2.21472×10^{13}
5	6393.41	6380.48	7060.58	7058.77	1.70595×10^{14}	1.74199×10^{14}	2.27782×10^{13}	2.31095×10^{13}
6	6391.97	6379.05	7064.51	7062.60	1.70572×10^{14}	1.74169×10^{14}	2.39024×10^{13}	2.42208×10^{13}
7	6391.43	6378.49	7071.53	7069.53	1.70584×10^{14}	1.74174×10^{14}	2.51505×10^{13}	2.54572×10^{13}
8	6391.04	6378.08	7079.91	7077.81	1.70649×10^{14}	1.74229×10^{14}	2.65037×10^{13}	2.67998×10^{13}
9	6394.31	6381.29	7090.97	7088.76	1.71267×10^{14}	1.74844×10^{14}	2.78286×10^{13}	2.81127×10^{13}
10	6397.94	6384.87	7102.90	7100.58	1.71966×10^{14}	1.75539×10^{14}	2.91842×10^{13}	2.94573×10^{13}
11	6402.03	6388.89	7117.89	7115.47	1.72748×10^{14}	1.76317×10^{14}	3.05707×10^{13}	3.08335×10^{13}

[†] The transition of the lines are $K\alpha_1$ ($2p_{3/2} \rightarrow 1s$), $K\alpha_2$ ($2p_{1/2} \rightarrow 1s$), $K\beta_1$ ($3p_{3/2} \rightarrow 1s$), and $K\beta_3$ ($3p_{1/2} \rightarrow 1s$). The nomenclatures follow Hölzer et al. (1997); Palmeri et al. (2003).

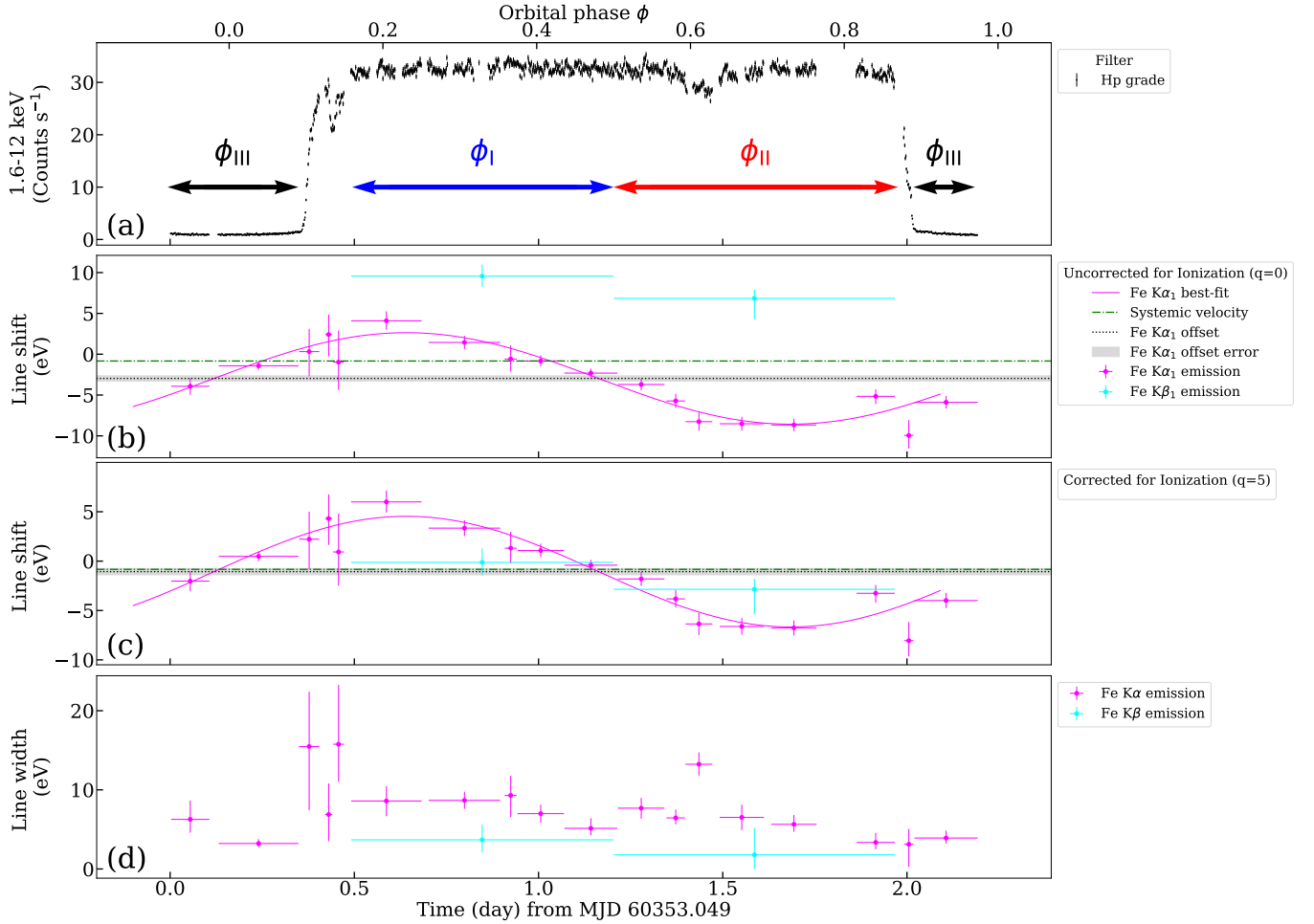


Fig. 1. (a) X-ray count rate, (b and c) RV curves of the Fe K α (magenta) and K β (cyan) line before and after the ionization correction, and (d) their Gaussian width. The MJD is given at the bottom, while the orbital phase at the top. In panel (a), Hp events in the 1.6–12 keV are binned at every 128 s. The three phases (ϕ_I , ϕ_{II} , and ϕ_{III}) are defined with arrows. In panel (b) and (c), the green dashed-and-dotted line is the systemic velocity of Cen X-3 (Hutchings et al. 1979). Panel (b) assumes that the lines are from neutral Fe ($q = 0$), while panel (c) is corrected for the ionization effect assuming that they are from Sc-like Fe ($q = 5$).

Alt text: Four stacked line graphs with a common x-axis showing MJD and orbital phase. The y-axis shows count rate in the top panel, line shift in the middle panels, and line width in the bottom panel.

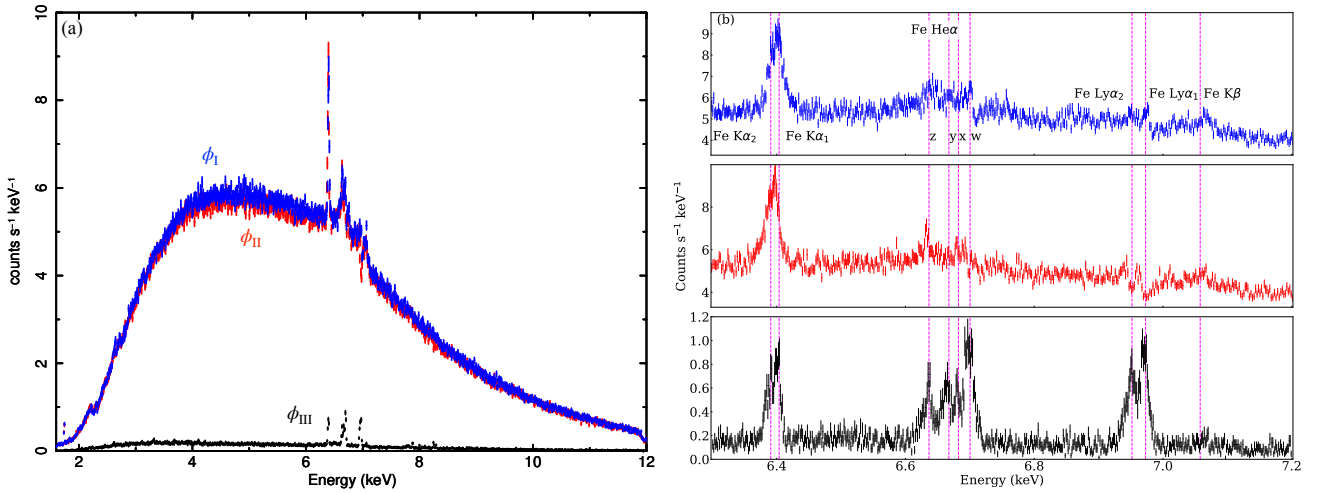


Fig. 2. (a) Broadband spectra of *Resolve* in three different phases obtained during the orbital phases ϕ_I (blue), ϕ_{II} (red) and ϕ_{III} (black). (b) Close-up view of each orbital-phase-resolved spectrum in the Fe K band, shown in the same color as panel a. The laboratory rest-frame energy of the Fe K lines are shown with the vertical magenta lines.

Alt text: Two line graphs show count versus energy. The right panel is divided into three vertical sections.

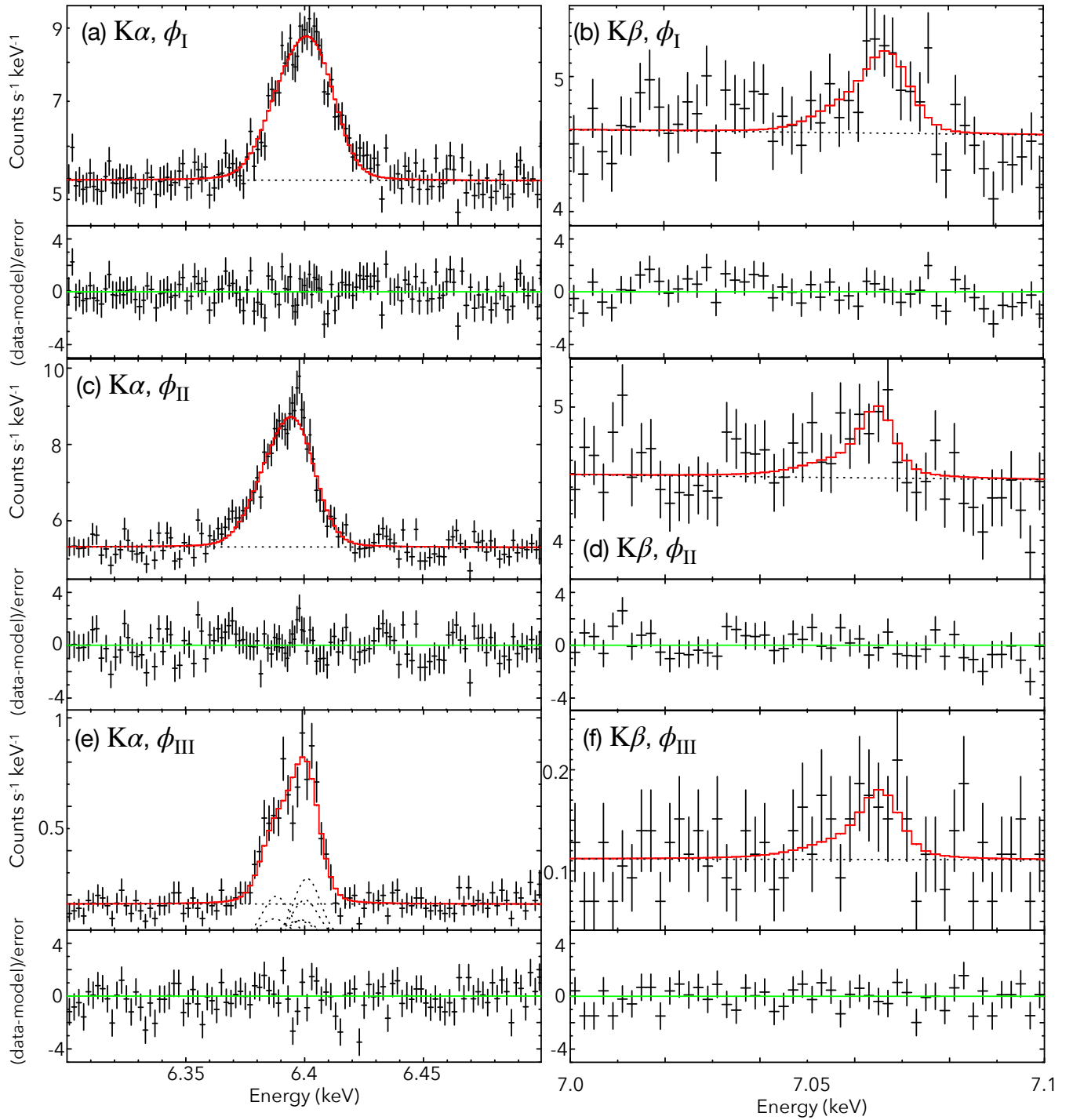


Fig. 3. Fitting results of the Fe K α (left panels) and Fe K β (right panels) lines for the three phases (top: ϕ_I , middle: ϕ_{II} , and bottom: ϕ_{III}). In each panel, the data (black) and the best-fit model (red) are shown at the top, while the fitting residual at the bottom. Panels (a)-(b), (c)-(d), and (e)-(f) show the K α and K β lines at ϕ_I , ϕ_{II} , and ϕ_{III} , respectively.

Alt text: Six line graphs for the K α and K β lines in the three phases. Each panel shows the spectrum and residual to the best-fit model.

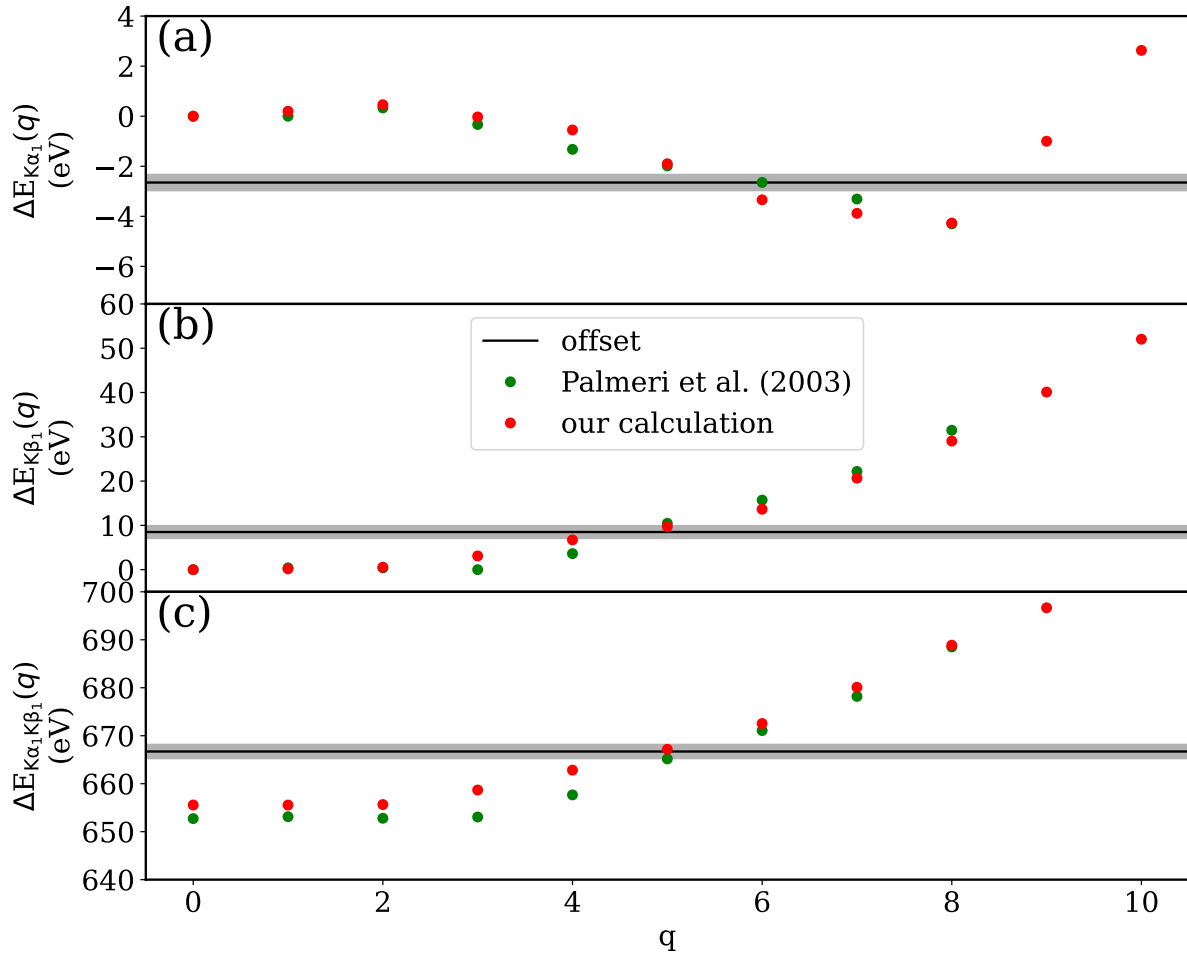


Fig. 4. Line energy shift of (a) K α_1 and (b) K β_1 relative to the neutral value, and (c) their differences as a function of the ionization degree q . Two theoretical calculations, Palmeri et al. (2003) and this work (RLSDA/SIC), are shown in red and green, respectively. In the former, numerous lines in the unresolved transition array were averaged by weighting with the fluorescence yield and the results up to $q = 8$ is available. In the latter calculation, a single Slater determinant was adopted without explicitly resolving angular-momentum coupling as in the configuration-interaction calculations. The resulting line energies therefore represent statistical-weighted averages over all allowed transitions, rather than those of any specific single transition. The energy difference of the initial and final orbitals are used up to $q = 11$ (table 3). The horizontal black line and gray region show the observed RV offset and its 1σ uncertainty.

Alt text: Three line graphs with a common x-axis showing the ionization degree. The y-axis shows the energy difference in the top, middle, and bottom panels.

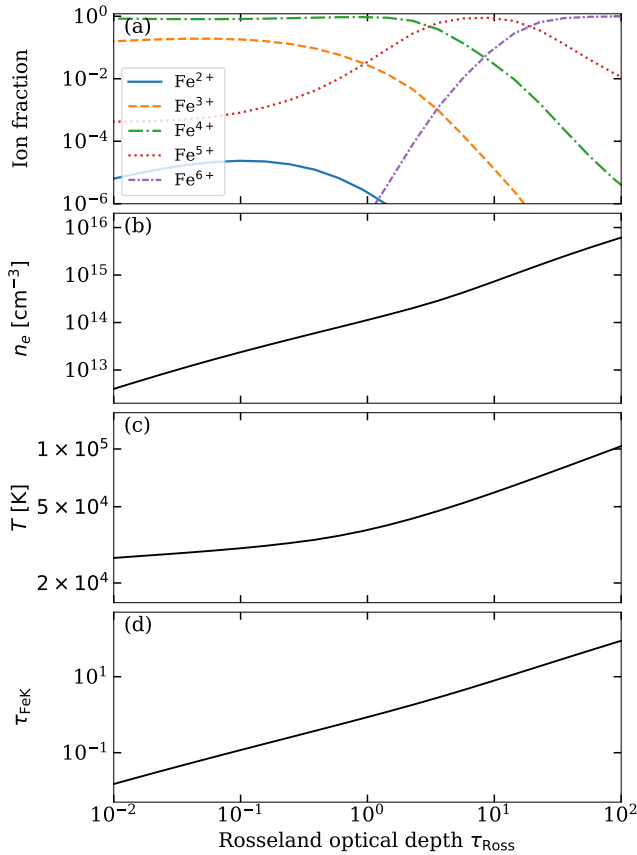


Fig. 5. Visualization of the atmosphere model calculation for the effective temperature of 3.5×10^4 K and the surface gravity of $10^{3.5}$ times of the solar value (Lanz & Hubeny 2003): (a) the Fe charge state distribution, (b) electron density, (c) temperature, and (d) the Fe K optical depth (τ_{FeK}) are shown as a function of the Rosseland optical depth (τ_{Ross}) as a proxy for the geometrical depth (z) from the surface. Here, τ_{Ross} is the Rosseland mean optical depth, increasing inward from the stellar surface ($\tau_{\text{Ross}} = 0$) toward deeper atmospheric layers. The data are available online at <https://tlusty.oce.eu/tlusty/Tlusty2002/tlusty-frames-0S02.html>. Alt text: Four line graphs for O star atmosphere model for the ion charge state distribution, electron density, temperature, and Fe K optical depth as a function of Rosseland optical depth.

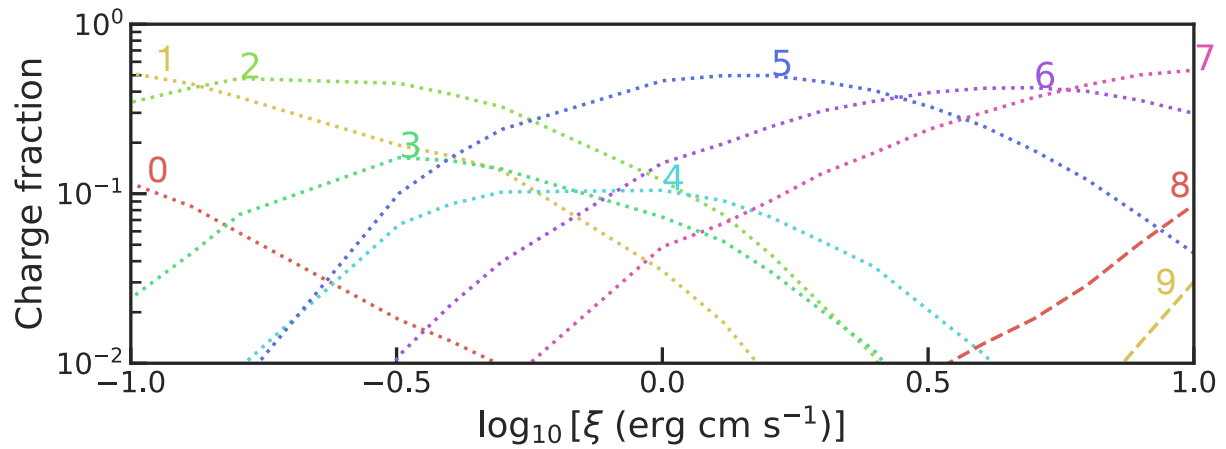


Fig. 6. Charge state distribution (CSD) of Fe as a function of the ionization parameter ξ calculated using xSTAR. The number q correspond to the Fe^{q+} ion. The NS spectrum of a power-law shape (photon index of 1.4) attenuated by a 10^{22} cm^{-2} column representing the stellar wind is used as the photoionizing source. Alt text: One line graph for the NS photoionization. The x-axis shows the photoionization parameter, and the y-axis shows the charge fraction of iron.

References

Aschenbrenner, P., Przybilla, N., & Butler, K. 2023, A&A, 671, A36

Ash, T. D. C., Reynolds, A. P., Roche, P., Norton, A. J., Still, M. D., & Morales-Rueda, L. 1999, MNRAS, 307, 357

Bearden, J. A. 1967, Rev. Mod. Phys., 39, 78

Berger, M. J., Hubbell, J. H., Seltzer, S. M., Chang, J., Coursey, J. S., Sukumar, R., Zucker, D. S., & Olsen K. 2010, NIST Standard Reference Database 8

Bildsten, L., et al. 1997, ApJS, 113, 367

Bogensberger, D., et al. 2025, PASJ, 77, S209

Chakraborty, P., et al. 2025, ApJ, 991, 224

Eckart, M. E., et al. 2025, JATIS, 11, 4, 042018

Eggleton, P. P. 1983, ApJ, 268, 368

Falanga, M., Bozzo, E., Lutovinov, A., Bonnet-Bidaud, J. M., Fetisova, Y., & Puls, J. 2015, A&A, 577, A130

Firestone, R. B., & Shirley, V. S. ed. 1996, Table of Isotopes Eighth Edition Volume II (New York: Wiley), F-41

Griffin, D. C., Andrew, K. L., & Cowan, R. D. 1969, Phys. Rev., 177, 62

Gunasekera, C. M., van Hoof, P. A. M., Tsujimoto, M., & Ferland, G. J. 2025, A&A, 694, L13

Hayashi, T., Mori, H., Mukai, K., Terada, Y., & Ishida, M. 2023, ApJ, 953, 30

Hayashi, T., et al. 2024, Proc. SPIE, 13093, 130931L

Hölzer, G., Fritsch, M., Deutsch, M., Härtwig, J., & Förster, E. 1997, Phys. Rev. A, 56, 4554

Hutchings, J. B., Cowley, A. P., Crampton, D., van Paradijs, J., & White, N. E. 1979, ApJ, 229, 1079

Ishisaki, Y., et al. 2025, JATIS, 11, 4, 042023

Kaastra, J. S. 1999, in X-Ray Spectroscopy in Astrophysics, ed. J. van Paradijs & J. A. M. Bleeker (Berlin: Springer), 269

Kallman, T., & Bautista, M. 2001, ApJS, 133, 221

Kammoun, E., et al. 2025, ApJL, 994, L13

Kelley, R. L., et al. 2025, JATIS, 11, 4, 042026

Kotchigova, S., Levine, Z. H., Shirley, E. L., Stiles, M. D., & Clark, C. W. 1997, Phys. Rev. A, 55, 191

Kramida, A., Ralchenko, Yu., Reader, J., and NIST ASD Team 2024, NIST Atomic Spectra Database (ver. 5.12)

Krzeminski, W. 1974, ApJL, 192, L135

Lanz, T. & Hubeny, I. 2003, ApJS, 146, 417

Leutenegger, M. A. et al. 2025, JATIS, 11, 4, 042024

Miller, J. M., et al. 2025, ApJL, 985, L41

Mochizuki, Y., et al. 2024, ApJL, 977, L21

Mochizuki, Y., et al. 2025a, JATIS, 11, 042002

Mochizuki, Y., et al. 2025b, PASJ, 77, S63

Naik, S., Paul, B., & Ali, Z. 2011, ApJ, 737, 79

Palmeri, P., Mendoza, C., Kallman, T. R., Bautista, M. A., & Meléndez, M. 2003, A&A, 410, 359

Perdew, J. P., & Zunger, A. 1981, Phys. Rev. B, 23, 5048

Porter, F. S., et al. 2025, JATIS, 11, 042016

Roos, C. E. 1957, Phys. Rev., 105, 931

Sanjurjo-Ferrín, G., Torrejón, J. M., Postnov, K., Oskinova, L., Rodes-Roca, J. J., & Bernabeu, G. 2021, MNRAS, 501, 5892

Tamba, T., Odaka, H., Tanimoto, A., Suzuki, H., Takashima, S., & Bamba, A. 2024, ApJ, 984, 126

Tarter, C. B., Tucker, W. H., & Salpeter, E. E. 1969, ApJ, 156, 943

Tashiro, M., et al. 2025, PASJ, 77, S1

Tong, X.-M., & Chu, S.-I. 1997, Phys. Rev. A, 55, 3406

Tong, X.-M., & Chu, S.-I. 1998, Phys. Rev. A, 57, 855

Tsygankov, S. S., et al. 2022, ApJL, 941, L14

Wilms, J., Allen, A., and McCray, R. 2000, ApJ, 542, 914

Wojdowski, P. S., Liedahl, D. A., & Sako, M. 2001, ApJ, 547, 973

XRISM Collaboration, et al. 2024, ApJL, 973, L25

Yamaguchi, H., et al. 2014, ApJ, 780, 136